Excerpt from the Proceedings of the 2011 COMSOL Conference in Stuttgart

Super-resolution Properties of the Maxwell Fish-Eye

D. Grabovičkić *, J. C. González, J. C. Miñano, P. Benítez
CEDINT, Universidad Politecnica de Madrid, Campus de Montegancedo 28223 Pozuelo, Madrid, Spain
*dejan@cedint.upm.es

Abstract: In this paper we present an analysis that shows the Maxwell Fish Eye (MFE) only has super-resolution property for some particular frequencies (for other frequencies, the MFE behaves as conventional imaging lens). These frequencies are directly connected with the Schumann resonance frequencies of spherical symmetric systems. The analysis have been done using a thin spherical waveguide (two concentric spheres with constant index between them), which is a dual form of the MFE (the electrical fields in the MFE can be mapped into the radial electrical fields in the spherical waveguide). In the spherical waveguide the fields are guided inside the space between the concentric spheres. A microwave circuit comprising three elements: the spherical waveguide, the source and the receiver (two coaxial cables) is designed in COMSOL. The super-resolution is demonstrated by calculation of Scaterring (S) parameters for different position of the coaxial cables and different frequencies of the input signal.

Keywords: Super-resolution, Maxwell fish-eye, Geodesic lens

1. Introduction

"Perfect imaging" stands for the capacity of an optical system to produce images with details unlimited by the wavelength of light. Perfect imaging has been theoretically demonstrated in the last decade using materials with negative dielectric and magnetic constants [1][2]. The super-resolution (i.e., objects resolved below the diffraction limits) based on these materials has been shown experimentally [3][4], as well. Unfortunately, high absorption and small (wavelength scale) source-to-image distance are inevitable in negative refraction [5].

Recently, a new possibility for perfect imaging has been proposed using a material with a positive, isotropic and gradient refractive index: the Maxwell Fish Eye (MFE) lens. It is well known that, in the Geometrical Optics framework, the MFE perfectly focuses rays emitted by an arbitrary point of space onto another (its image point). Leonhardt [6] demonstrated that the MFE lens in two dimensions (2D) perfectly focuses radiation of any frequency between the source and its image for 2D Helmholtz fields (which describes TE-polarized modes in a cylindrical MFE, i.e., in which electric field vector points orthogonal to the cross section of the cylinder); this result has also been confirmed via a different approach [7].

This "perfect focusing" stands for the capacity of an optical system to perfectly transport an outward (monopole) 2D Helmholtz wave field, generated by a point source, towards an "infinitely-well localized drain" (which we will call "perfect point drain") located at the corresponding image point. That perfect point drain must be able to absorb totally all incident radiation, with no reflection or scattering, and the field around the drain asymptotically coincides with an inward (monopole) wave. Perfect focusing occurs in the MFE using perfect drains for an arbitrary frequency if they are located at the image point of the source.

In this paper we present the results of the super-resolution analysis for microwaves of the Spherical Geodesic Waveguide (SGW), a device suggested in [14]. It is obtained via transformation optics from a MFE planar waveguide. The SGW is a spherical waveguide filled with a non-magnetic material and isotropic refractive index distribution proportional to $1/r$ ($\varepsilon=(r_0/r)^2$ and $\mu=1$), r being the distance to the center of the spheres. Transformation Optics theory [16] proves that the TE-polarized electric modes of the cylindrical MFE [6] are transformed into radial-polarized modes in the SGW, so both have the same perfect focusing properties.

When the waveguide thickness is small, the variation of the refractive index within the two spherical shells can be ignored resulting in a constant refractive index within the waveguide.

Here, we have obtained that super-resolution only occurs close to the discrete set

of Schumann frequencies. Also it is demonstrated that the use of the perfect drain is not necessary.

2. Spherical Geodesic Waveguide

The Maxwell Fish-Eye (MFE) lens is a positive, isotropic and radial refractive-index which provides perfect imaging between two points in a plane, i.e., the rays issuing from a point (x_0, 0) are perfectly focused at another point (a^2/x_0, 0). A cylindrical MFE is a lens with the following refraction index distribution:

$$n(\rho) = \frac{2n_0}{1+(\rho/a)^2} \qquad (1)$$

where ρ is the distance to the origin. Leonhardt found that this perfect focusing property also holds in z-polarised waves [6]. The wave propagating (Leonhard's forward wave [8]) from object point (x_0, 0) into image point (a^2/x_0, 0), is given by

$$\mathbf{E}(x,y,z) = A\left(P_\nu(\zeta) + i\frac{2}{\pi}Q_\nu(\zeta)\right)\mathbf{z}$$
$$\zeta = \frac{|z'|^2 - a^2}{|z'|^2 + a^2} \qquad z' = \frac{z - x_0}{z\frac{x_0}{a^2}+1} \qquad (2)$$

Here A is a complex constant, $P\upsilon$, $Q\upsilon$ are the Legendre functions [12], and z is a complex number defined as $z=x+iy$.

Using Transformation Optics it was proven [14] that the fields given by Eq. (2) in a 2D MFE are transformed into radial fields in the SGW filled with a refractive index medium with law $n(r) = an_0/r$ (where $r^2=x^2+y^2+z^2$). The radial field $\mathbf{E}(r,\theta,\phi)=E_r(r,\theta,\phi)\mathbf{r}$ in the SGW is related to the MFE field (Eq. (2)) of the corresponding point by:

$$E_r(r,\theta,\phi) = E_z(\zeta) \quad \zeta = \cos\theta \qquad (3)$$

Corresponding points in the MFE and SGW are related by a stereographic projection. Source and drain points (x_0,0) and ($-a^2/x_0$,0) are transformed into opposite poles of the SGW. Leonhardt's forward wave is transformed into a wave with rotational symmetry with respect to the line passing through object and image points.

The SGW is bounded by two spherical shells made of conductors. Two coaxial probes loaded with their characteristic impedance have been used to simulate the source and drain in the SGW. The microwave prototype described in [10] and [11] was done in the same way. We will call them source port and drain port respectively. Both ports are geometrically identical. The drain port is loaded with its characteristic impedance Zo. The drain, (when is located at the image point) is not perfect, since it causes a reversed wave, as well [9]. Although there is no perfect focusing as defined before (i.e. full absorption of the forward wave), the SGW "senses" small shifts (much smaller than wavelength) indicating super-resolution (see Section 3.). This has practical interest since there is no need for perfect drains [9].

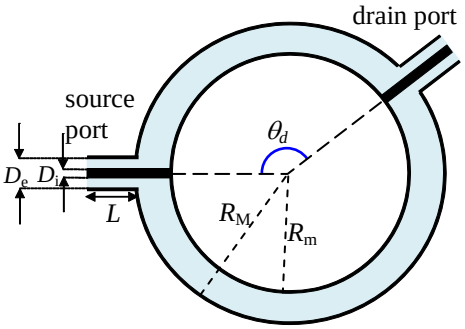

Figure 1. Cross section of the two coaxial lines and the spherical waveguide (SGW). The power is injected through the source port, The radiation is guided between spheres and may be extracted at the drain port.

Figure 1. shows the cross section of the SGW with the two coaxial probes simulating the point source and the point drain. The radiation is injected through the source port, guided between spheres, and may (or not) be extracted from the sphere through the drain port. When the angle $\theta_d = \pi$, the drain port is located at the image point and the fields will have rotational symmetry. For $\theta_d \neq \pi$, the rotational symmetry is broken.

The frequencies used in the analysis are low enough so only TEM modes propagate in the coaxial cables. Therefore, the complete system can be analyzed as a microwave circuit using the classical scattering matrix **S** [15]. Figure 2. shows the equivalent circuit.

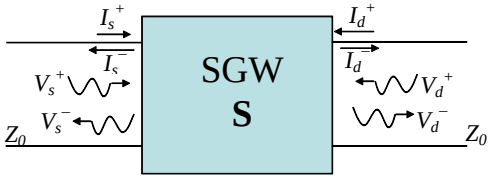

Figure 2. Microwave circuit made up of the two ports and the spherical waveguide. The sphere S completely characterized with the **S** matrix.

The matrix **S** of the sphere is defined as:

$$\begin{bmatrix} V_s^- \\ V_d^- \end{bmatrix} = \begin{bmatrix} S_{11} & S_{12} \\ S_{21} & S_{22} \end{bmatrix} \begin{bmatrix} V_s^+ \\ V_d^+ \end{bmatrix} \quad (4)$$

When the drain port is matched with its characteristic impedance *Zo*, there is no reflected wave in this coaxial line and thus the voltage and current waves Vd^+ and Id^+ are null:

$$\begin{aligned} V_d^- &= S_{21} V_s^+ \\ V_s^- &= S_{11} V_s^+ \end{aligned} \quad (5)$$

The power injected through the source port P_I, transmitted to the drain port P_T and reflected by it P_R are:

$$P_I = \frac{1}{2}\frac{|V_s^+|^2}{Z_o} \qquad P_T = P_I |S_{21}|^2$$
$$P_R = P_I (1 - |S_{21}|^2) \quad (6)$$

3. Simulations in COMSOL Multiphysics

The simulation has been done using 3D RF Modul in COMSOL Multiphysics. The SGW has been modeled with the following geometrical parameters (see Figure 1.):

$$D_e = 10\text{ mm} \quad D_i = 5\text{ mm} \quad L = 20\text{ mm}$$
$$R_M = 1005\text{ mm} \quad R_m = 1000\text{ mm} \quad (7)$$

The refractive index between the spherical shells should be $n(r)=an_0/r$. However, as commented before, since $R_M/R_m \approx 1$ we have made an approximate model having $n=1$ inside the waveguide.

The SGW model has been analyzed using a frequency range from 0.2 GHz to 0. 4 GHz (λ between 0.75 m and 1.5 m), which is well below the cut-off frequency of next higher order mode in the coaxial cables (the cut-off frequency ~$(2c/\pi)/(D_e+D_i)$ = 112.7 GHz [15]).

The port radius (D_e) is less than $\lambda/100$ for the analyzed frequencies and the ratio $D_e/R_m << 1$, which means that we have modeled the point nature of source and drain successfully. The coaxial lines are 20 mm long, which is enough to guarantee the evanescent modes in the coaxial lines are negligible at their ends. The conductor has been designed as a zero-thickness ideal metal sheet.

Special care has been taken to define the mesh of the system. In order to mesh the guide properly, the geometry has been divided into few domains. Each domain is meshed separately according to its geometric and physical properties. Since the guide thickness is very low $(R_M-R_m)/R_m << 1$, the SGW is meshed using a swept mesh (2D triangular mesh from the outer surface is swept to the inner surface, as presented in Figure 3.). On the other side, the coaxial cables are meshed with higher density using 3D tetrahedra. The mesh density is increased since the change of the Electrical field is significant in the neighbourhood of the coaxial cables.

(a)

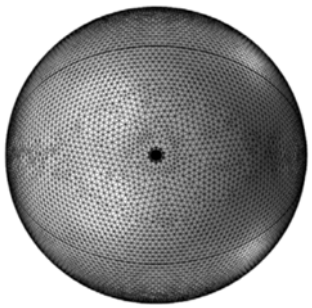

(b)

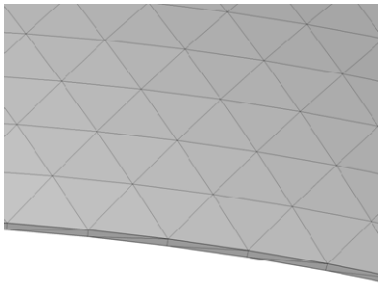

(c)

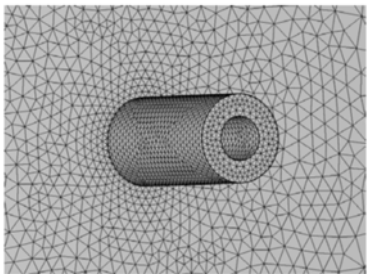

Figure 3. Mesh structure. (a) SGW with coaxial cables, (c) close up of a piece of spherical shells, (c) close up of one coaxial cable from outside the sphere

Several simulations have been made to analyze the imaging properties of the system. We have used $|S_{21}|^2$ to determine the sensitivity of the transmitted power P_T (which is proportional to $|S_{21}|^2$, see Eq. (6)) to the drain port position.

Figure 4. shows $|S_{21}|^2$ for a frequency range between 0.2 GHz and 0.4 GHz when the drain port is placed at the source's image point, that

is, θ =0 for the source port and θ =π for the drain port. There are peaks of $|S_{21}|^2$ indicating total transmission from the source port towards the drain port, resembling the transmission diagram of a Fabry-Pérot resonator (see for instance [17]). These peaks occur at the well-known Schumann resonance frequencies of the spherical systems [18], which correspond to integer values of ν from the next equation [9]

$$\left(R_M k_0\right)^2 = \nu(\nu+1) \qquad (8)$$

where $k_0 = 2\pi f\sqrt{\mu_0\varepsilon_0}$.

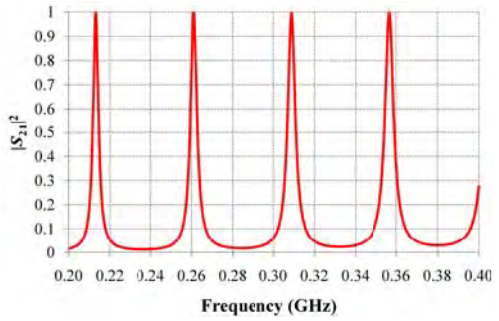

Figure 4. $|S_{21}|^2$ as function of frequency when the drain and source ports are at opposite poles. The peaks occur at the Schumann resonance frequencies.

Figure 5. shows $|S_{21}|^2$ when the drain port is shifted λ/30 (for λ=1m corresponding to 0.3 GHz) away of source port antipode. Although the results are extremely similar, narrow notches in the transmission very close to the Schumann frequencies occur. These notches are getting wider when the drain port is shifted further from the source's image point (see Figure 6.).

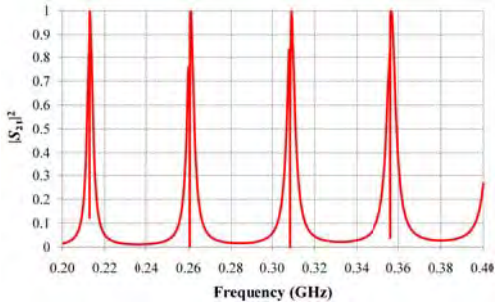

Figure 5. $|S_{21}|^2$ vs frequency when the drain port is shifted λ/30 (λ=1.15 m) from the source port antipode. The results are similar to those presented in Figure 4. in accordance with the classical prediction, except for the very narrow notches near Schumann frequencies.

Figure 6. shows $|S_{21}|^2$ for different drain port positions in a very narrow band in the neighborhood of the Schumann frequency corresponding to the second peak in Figure 5. (for which ν =5). The label of each curve indicates the distance between the drain port center and the source port antipode. The black curve corresponds to the drain port placed in the source port antipode (it looks flat because of the high zoom in the frequency axis). The other curves correspond to different shifts of the drain port. The shifts are in all cases much smaller than wavelength (λ=1.15084047 m that correspond to f=0.2606873 GHz). These results are quite surprising, since close to a specific frequency the power transmitted to the drain port suddenly reduces to a value near zero, indicating super-resolution.

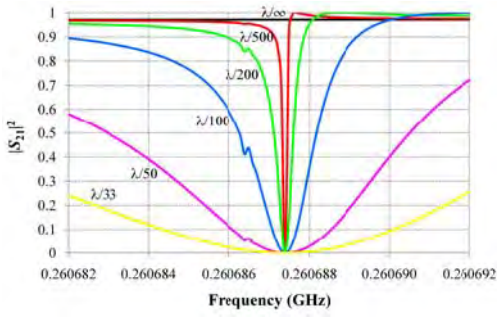

Figure 6. Detailed picture of $|S_{21}|^2$ as function of the frequency in a narrow band around a Schumann frequency for different drain port positions (the corresponding shift on the inner sphere of the SGW between the drain port centre and the source port antipode has been used for labelling).

Figure 7. shows the same information as Figure 6. but plotting $|S_{21}|^2$ vs the drain port shift (expressed in units of λ) and using the frequency as a parameter. All the chosen frequencies are slightly above the Schumann frequency (graphs for frequencies slightly below are quite similar).

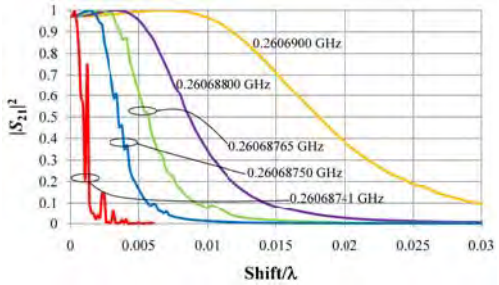

Figure 7. $|S_{21}|^2$ as function of the drain port shift for different frequencies that present super-resolution of between λ/30 and λ/500.

Let us define "resolution" as the arc length that drain port needs to be shifted so $|S_{21}|^2$ drops to 10%. From the orange to the red curves, increasing super-resolutions are

achieved: 0.03 λ (that is, λ/33) for the orange to λ/500 for the red. The latter, whose frequency f=0.26068741 GHz corresponds to ν=4.99636) is the highest resolution that we have obtained. Computations for frequencies closer ν=5 show essentially null $|S_{21}|^2$ values for shifts > λ/500 (as in the red line in the picture), but also instabilities in the $|S_{21}|^2$ values for shifts below λ/500.

Clearly from Figure 6., one concludes that the higher the resolution, the narrower the bandwidth. The bandwith has been calculated as f_{max}–f_{min} with f_{max} and f_{min} fulfilling $|S_{21}(f_{max})|^2=|S_{21}(fmin)|^2=0.1$.

The λ/500 resolution is achieved inside a narrow bandwidth of 20 Hz. The lowest resolution presented in Figure 6. (the λ/33 resolution) is obtained inside a bandwidth of 5810 Hz.

4. Conclusions

Simulations of the spherical waveguide (SGW) show super-resolution up to λ/500 (near to the Schumann frequency). However, it is obtained only inside a narrow band (width ≈ 20 Hz). If larger bandwidths are needed, lower resolutions (but still sub-wavelength) are achieved. Far from a Schumann frequency, no super-resolution is observed. The super-resolution is achieved using an approximate model of the SGW (the model having n=1 inside the waveguide) without perfect drain. This is obviously very attractive from the practical point of view. The waveguide can be manufactured with just two concentric metallic spheres separated at a distance much less than the radius and constant refraction index between them.

5. References

1. J. B. Pendry, Negative Refraction makes a Perfect Lens, *Phy. Review Let.* **85** 3966-3989 (2000)
2. R. A. Shelby et al, Experimental verification of negative index of refraction, *Science*, **292**, 79 (2001)
3. N Fang et al, Sub-Diffraction-Limited Optical Imaging with a Silver Superlens, *Science*, **308**, 534-537 (2005)
4. F Mesa et al, Three dimensional superresolution in material slab lenses: Experiment and theory, *Phy. Review B* **72**, 235117 (2005)
5. M. I. Stockman, Criterion for Negative Refraction with Low Optical Losses from a Fundamental Principle of Causality, *Physical Review Letters*, **98**, 177404 (2007)
6. U. Leonhardt, Perfect imaging without negative refraction, *New J. Phys.*, **11**, 093040 (2009)
7. P. Benítez et al, 2010 Perfect focusing of scalar wave fields in three dimensions, *Optics Express*, **18**, 7650-7663 (2010)
8. J.C González et al, Perfect drain for the Maxwell Fish Eye lens, *New Journal of Physics* (2011)
9. J.C Miñano et al, Super-resolution for a point source better than λ/500 using positive refraction, *ArXiv:1101.2978v3* (2011)
10. YG Ma et al, Perfect imaging without negative refraction for microwaves, *ArXiv:1007.2530v1* (2010)
11. YG Ma et al, Evidence for subwavelength imaging with positive refraction, *New Journal of Physics*, (2011)
12. A. Erdélyi et al, *Higher Transcendental Functions vol I* , New York: McGraw-Hill (1953)
13. R.K Luneburg, *Mathematical theory of optics.* University of California Press (1964).
14. J.C Miñano et al, Perfect imaging with geodesic waveguides. *New Journal of Physics*, **12**, 123023 (2010)
15. M. Pozar David, *Microwave Engineering*. John Wiley&Son In (2005).
16. U. Leonhardt, *Geometry and Light: The Science of Invisibility*, Dover (2010)
17. S. Solimeno et al, *Guiding, Diffraction and Confinement of Optical Radiation*, Academic (1986)
18. D.J. Jackson, *Classical Electrodynamics* John Wiley & Sons, Inc. (1998)

6. Acknowledgments

The authors thank the Spanish Ministry MCEI (Consolider program CSD2008-00066, DEFFIO: TEC2008-03773), TEC2010-16948) for the support given in the preparation of the present work.